

Using a structural root system model to evaluate and improve the accuracy of root image analysis pipelines.

1 **Guillaume Lobet**^{1,2,*,+}, **Iko T. Koevoets**^{3,+}, **Manuel Noll**^{1,+}, **Patrick E. Meyer**¹, **Pierre Tocquin**¹,
2 **Loïc Pagès**⁴, **Claire Périlleux**¹

3 ¹ InBioS-PhytoSYSTEMS, University of Liège, 4000 Liège, Belgium

4 ² Institut für Bio-und Geowissenschaften: Agrosphäre, Forschungszentrum Jülich, D52425 Jülich,
5 Germany

6 ³ Plant Cell Biology, Swammerdam Institute for Life Sciences, University of Amsterdam, 1098 XH
7 Amsterdam, The Netherlands

8 ⁴ INRA, Centre d'Avignon, UR 1115 PSH, Site Agroparc, 84914 Avignon cedex 9, France

9 ⁺ These authors contributed equally to this work

10 *** Correspondence:**
11 Corresponding Author
12 g.lobet@fz-juelich.de

13 **Keywords: image analysis, root structural model, benchmarking, image library, machine**
14 **learning.**

15 **Abstract**

16 Root system analysis is a complex task, often performed with fully automated image analysis
17 pipelines. However, the outcome is rarely verified by ground-truth data, which might lead to
18 underestimated biases.

19 We have used a root model, ArchiSimple, to create a large and diverse library of ground-truth root
20 system images (10,000). For each image, three levels of noise were created. This library was used to
21 evaluate the accuracy and usefulness of several image descriptors classically used in root image
22 analysis softwares.

23 Our analysis highlighted that the accuracy of the different traits is strongly dependent on the quality
24 of the images and the type, size and complexity of the root systems analysed. Our study also
25 demonstrated that machine learning algorithms can be trained on a synthetic library to improve the
26 estimation of several root system traits.

27 Overall, our analysis is a call to caution when using automatic root image analysis tools. If a
28 thorough calibration is not performed on the dataset of interest, unexpected errors might arise,
29 especially for large and complex root images. To facilitate such calibration, both the image library
30 and the different codes used in the study have been made available to the community.

31

32 1 Introduction

33 Roots are of utmost importance in the life of plants and hence selection on root systems represents
34 great promise for improving crop tolerance to biotic and abiotic stresses (as reviewed in (Koevoets et
35 al., 2016). As such, their quantification is a challenge in many research projects. This quantification
36 is usually twofold. The first step consists in acquiring images of the root system, either using classic
37 imaging techniques (CCD cameras) or more specialized ones (microCT, X-Ray, fluorescence, ...).
38 The next step is to analyse the pictures to extract meaningful descriptors of the root system.

39 To paraphrase the famous Belgian surrealist painter, René Magritte: “figure 1A is not a root system”.
40 Figure 1A is an image of a root system and that distinction is important. an image is indeed a two-
41 dimensional representation of an object, which is usually three-dimensional. Nowadays,
42 measurements are generally not performed on the root systems themselves, but on the images, and
43 this raises some issues.

44

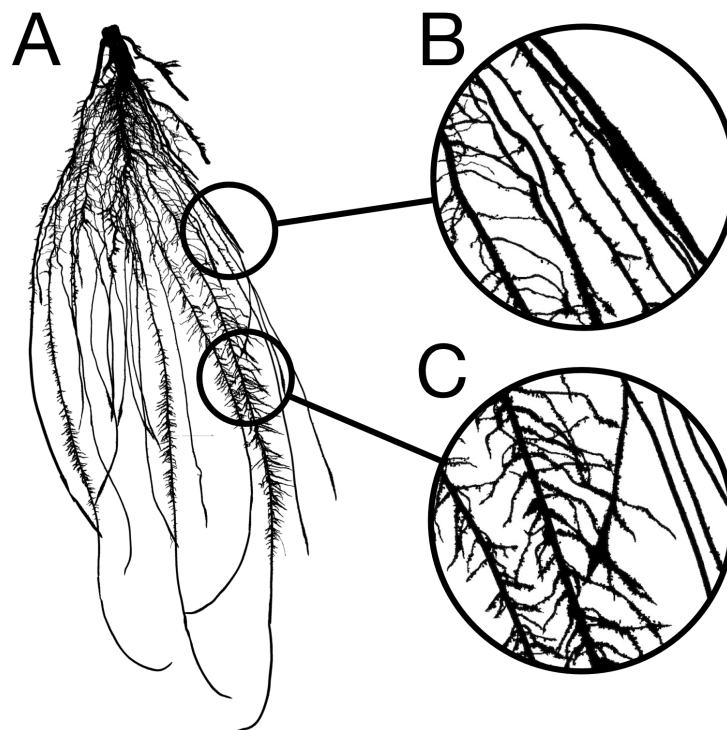


Figure 1. A. Image of a 2-week old maize root system grown in rhizotron. B. Close-up showing overlapping roots. C. Close-up showing crossing roots.

45

46 Image analysis is the acquisition of traits (or descriptors) describing the objects contained in a
47 particular image. In a perfect situation, these descriptors would accurately represent the biological
48 object of the image with negligible deviation from the biological truth (or data). However, in many
49 cases, artefacts might be present in the images so that the representation of the biological object is not
50 accurate anymore. These artefacts might be due to the conditions under which the images were taken
51 or to the object itself. Mature root systems, for instance, are complex branched structures, composed

52 of thousands of overlapping (fig. 1B) and crossing segments (fig. 1C). These features are likely to
53 impede image analysis and create a gap between the descriptors and the data.

54 Root image descriptors can be separated into two main categories: morphological and geometrical
55 descriptors. Morphological descriptors refer to the shape of the different root segments forming the
56 root system (table 1). They include, among others, the length and diameter of the different roots. For
57 complex root system images, morphological descriptors are difficult to obtain and are prone to error
58 as mentioned above. Geometrical descriptors give the position of the different root segments in
59 space. They summarize the shape of the root system as a whole. The simplest geometrical descriptors
60 are the width and depth of the root system. Since these descriptors are mostly defined by the external
61 envelope of the root system, crossing and overlapping segments have little impact on their estimation
62 and hence they can be considered as relatively errorless. Geometrical descriptors are expected to be
63 loosely linked to the actual root system topology, since identical shapes could be obtained from
64 different root systems (the opposite is true as well). They are usually used in genetic studies, to
65 identify genetic bases of root system shape and soil exploration.

66 Several automated analysis tools were designed in the last few years to extract both types of
67 descriptors from root images (Armengaud et al., 2009; Bucksch et al., 2014; Galkovskyi et al., 2012;
68 Pierret et al., 2013). However, the validation of such tools is often incomplete and/or error prone. For
69 technical reasons, the validation is usually performed on a small number of ground-truth images of
70 young root systems. In agreement, most analysis tools are specifically designed for this kind of root
71 systems. In the few cases where validation is performed on large and complex root systems, it is
72 usually not on ground-truth images, but in comparison with previously published tools (measurement
73 of X with tool A compared with the same measurement with tool B). This might seem reasonable
74 approach regarding the scarcity of ground-truth images of large root systems. However, the inherent
75 limitations of these tools, such as scale or root system type (fibrous- vs. tap-roots) are often not
76 known. Users might not even be aware that such limitations exist and apply the provided algorithm
77 without further validation on their own images. This can lead to unexpected errors in the final
78 measurements.

79 One strategy to address the lack of in-depth validation of image analysis pipelines would be to use
80 synthetic images generated by structural root models (models designed to recreate the physical
81 structure and shape of root systems). Many structural root models have been developed, either to
82 model specific plant species (Pagès et al., 1989), or to be generic (Pagès et al., 2004; 2013). These
83 models have been repeatedly shown to faithfully represent the root system structure (Pagès and
84 Pellerin, 1996). In addition, they can provide the ground-truth data for each synthetic root system
85 generated, independently of its complexity. However, they have not been used for validation of
86 image analysis tools (Rellán-Álvarez et al., 2015), with one exception performed on young seedling
87 unbranched roots (Benoit et al., 2014),.

88 Here we (i) illustrate the use of a structural root model, Archisimple, to systematically analyse and
89 evaluate an image analysis pipeline and (ii) use the model-generated images to improve the
90 estimation of root traits.

91

92 2 Material and methods

93 2.1 Nomenclature used in the paper

94 - **Ground-truth data:** The real (geometrical and morphometrical) properties of the root system as a
95 biological object. They are determined by either manual tracking of roots or by using the output of
96 simulated root systems.

97 - **(Image) Descriptor:** Property of the root image. It does not necessarily have a biological meaning.

98 - **Root axes:** first order roots, directly attached to the shoot

99 - **Lateral roots:** second- (or lower) order roots, attached to another root

100

101 2.2 Creation of a root system library

102 We used the model ArchiSimple, which was shown to allow the generation of a large diversity of
103 root systems with a minimal amount of parameters (Pagès et al., 2013). In order to produce a large
104 library of root systems, we ran the model 10,000 times, each time with a random set of parameters
105 (fig. 2A). For each simulation, the growth and development of the root system were constrained in
106 two dimensions.

107 The simulations were divided into two main groups: fibrous and tap-rooted. For the fibrous
108 simulations, the model generated a random number of root axes and secondary (radial) growth was
109 disabled. For tap-root simulations, only one root axis was produced and secondary growth was
110 enabled (the extent of which was determined by a random parameter).

111 The root system created in each simulation was stored in a Root System Markup Language (RSML)
112 file. Each RSML file was then read by the RSML Reader plugin from ImageJ to extract ground-truth
113 data for the library (Lobet et al., 2015). These ground-truth data included geometrical and
114 morphological parameters (table 1). For each RSML data file, the RSML Reader plugin also created
115 three JPEG images (at a resolution of 300 DPI) for each root system, with different levels of noise
116 (using the Salt and Pepper Filter in ImageJ) (fig. 2.D). For each root system, we computed
117 overlapping index as the number of root segments having an overlap with other root segments over
118 the total number of root segments.

119 2.3 Root image analysis

120 Each generated image was analysed using a custom-made ImageJ plugin, Root Image Analysis-J (or
121 RIA-J). For each image, we extracted a set of classical root image descriptors, such as the total root
122 length, the projected area and the number of visible root tips (fig. 2E). In addition, we included shape
123 descriptors such as the convex-hull area or the exploration ratio (see Supplemental file 1 for details of
124 RIA-J). The list of traits and algorithms used by our pipeline is listed in table 2.

125

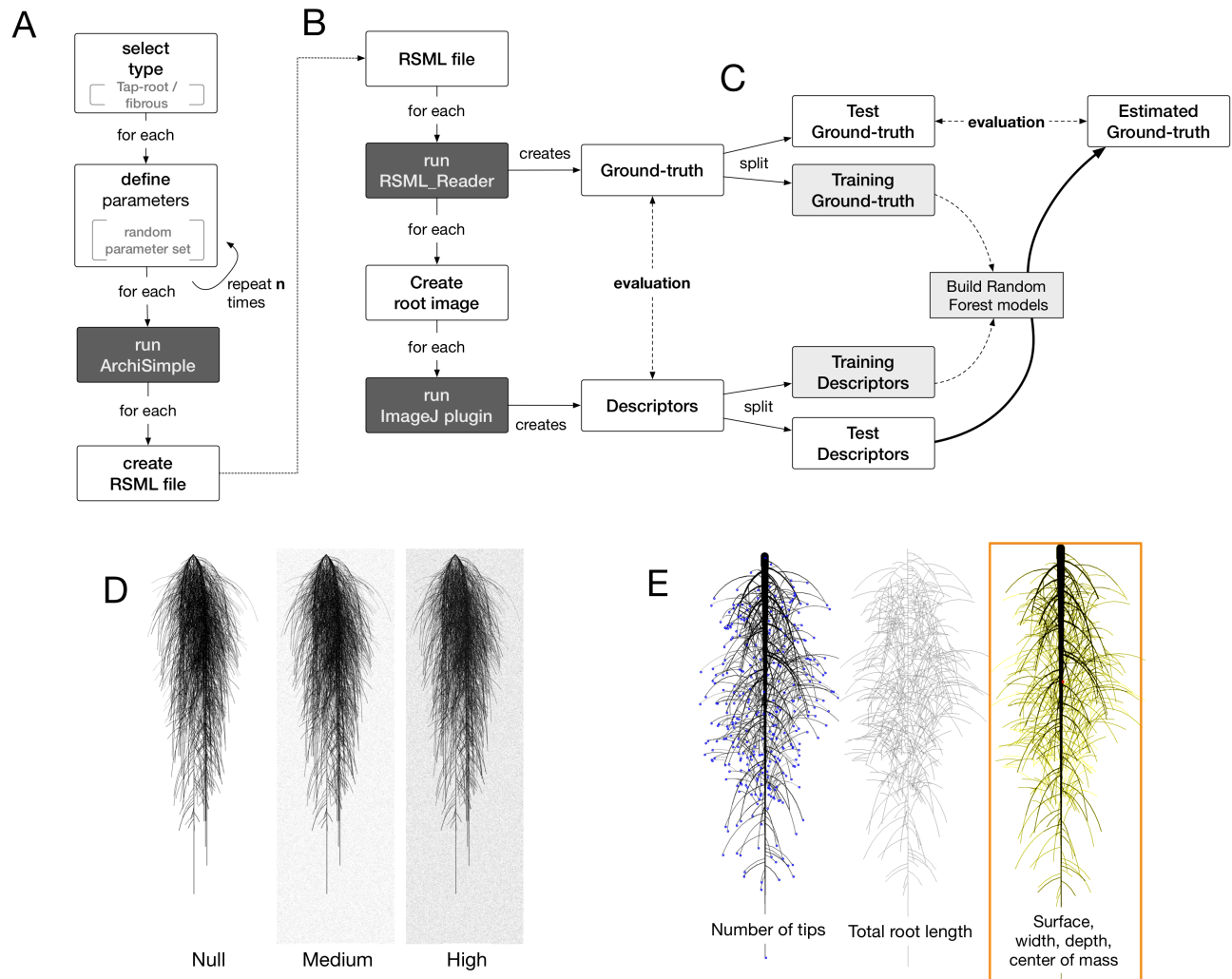


Figure 2: Overview of the workflow used in this study. A. Generation of root systems using Archisimple. B. Creation and analysis of root images. C. Use of Random Forest algorithms to better estimate root system ground-truths. D. Illustration of the different noise levels used in the analysis. E. Example of descriptors extracted with RIA-J

126

127

128 2.4 Data analysis

129 Data analysis was performed in R (R Core Team). Plots were created using *ggplot2* (Wickham, 2009)
 130 and *lattice* (Sarkar, 2008).

131 The Mean Relative Errors (MRE) were estimated using the equation:

132

$$MRE = \frac{\sum_1^n |\bar{y}_i - y_i|}{n}$$

133 where n is the number of observations, \bar{y}_i is the ground-truth and y_i is the estimated ground-truth.

134

135 2.5 Random Forest Framework

136 A *random forest* is a state-of-the-art machine learning algorithm typically used for making new
137 predictions (in both classification and regression tasks). Random Forests can perform non-linear
138 predictions and, thus, those often outperform linear models. Since its introduction by Breiman in
139 2001 (Breiman, 2001), those have been widely used in many fields from gene regulatory network
140 inference to generic image classification (Marée et al., 2016, Huynh-Thu et al., 2013). Random forest
141 relies on growing a multitude of decision trees, a prediction algorithm that has shown good
142 performances by itself but, when combined with other decision trees (hence the name forest), returns
143 predictions that are much more robust to outliers and noisy data (see bootstrap aggregating, Breiman
144 1996).

145 In a machine learning setting one is given a set $D = \{(x_1, y_1), (x_2, y_2), \dots, (x_n, y_n)\}$,

146 where $x_i = (x_i^1, x_i^2, \dots, x_i^s)$ is an element of a s –dimensional *feature space* X ,

147 and $y_i = (y_i^1, y_i^2, \dots, y_i^t)$ an element of a t –dimensional *response space* Y .

148 The learning task is to find a model

$$149 \quad M: X \rightarrow Y$$

150 that predicts the data in a good way, where goodness is measured w.r.t. an error function L .

151 A decision tree T_D is a machine learning method that, for a dataset D , constructs a binary tree with
152 each node representing a binary question and each leaf a value of the response space. In other words,
153 a prediction can be made from an input value by looking at the set of binary questions that leads to a
154 leaf (e.g. is the primary root bigger than q1 and if yes is the number of secondary roots smaller than
155 q2 and if no, ...)

156 Each decision is based upon exactly one feature and is used for deciding which branch of the tree a
157 given input value must take. Hence a decision tree splits successively the set D into smaller subsets
158 and assigns them a value $y_i = T_D(x_i)$ of the response space.

159 The choice of the feature used for splitting depends on a relevance criterion. In our setting, the
160 default relevance criterion from the randomForest R package (CRAN randomForest, 2015), namely
161 the Gini index, has been used.

162 A random forest

$$163 \quad F_D = (T_{D,k})_{k \in I} \text{ where } I = \{1, 2, \dots, l\}$$

164 consists of l decision trees $T_{D,k}$, where several key parameters such as the feature space, are chosen
165 randomly (hence the word Random in the algorithm name). While using a random subspace strongly
166 accelerates the growth of a single tree, it can also decrease its accuracy. However, the use of large
167 number of trees counterbalance advantageously those two effects. The final prediction for each input
168 value x_i corresponds to the majority vote of all the decision trees of the forest $T_{D,k}(x_i)$ in a classification
169 setting while an average of all predicted values is used in a regression task.

170 **2.5.1 Framework description**

171 Our method consists of three typical steps:

172 - a preprocessing step, where we replace missing values of the training set.

173 - a model generation step where, for each response variable, we generate different models according
174 to two Random Forest parameters (number of trees and number of splits).

175 - a model selection step, where we choose the best performing pair of parameters of the previous step
176 for each one of the response variable.

177 **2.5.2 Preprocessing**

178 Missing values in our dataset might arise due to highly noisy images, where the measurement of
179 certain descriptors has been infeasible. To deal with this issue, we first replaced missing values.

180 This is done using the imputation function of the randomForest R package. It replaces all missing
181 values of a response variable by the median and then a Random Forest is applied on the completed
182 data to predict a more accurate value. We favored ten trees for computing the new value over the
183 default value of 300 as we found that it offered sufficiently accurate results for our application while
184 being much faster.

185 **2.5.3 Model Generation**

186 In the model generation step, for each of the response variables, several forests with different number
187 of trees and different number of splits (t_i, m_j) are tested. In practice, the training set D_{train} is
188 divided into m_j disjunct subsets $D_{train}^{m_j}$ and on each of those, a random forest $F_{D_{train}^{m_j}}$ is trained on a
189 growing number of t_i random trees.

190

191 **2.5.4 Model selection**

192 Given a new data point x , each model predicts a response variable y by averaging the predicted
193 values $F_{D_{train}^m}(x)$, i.e.

194
$$\hat{y} = M_{D_{train}^{t,m}}(x) = \frac{1}{m} \sum_{k=1}^m F_{D_{train}^k}(x)$$

195 Then in a final step an estimate of the root-mean-square (RMSE) generalized error on the test set
196 D_{test} is computed, where RSME is defined as

197

198
$$RMSE = \sum_{i=1}^n \sqrt{(y_i - \bar{y}_i)^2}$$

199 for $D_{test} = \{(x_1, y_1), (x_2, y_2), \dots, (x_n, y_n)\}$.

200

201 Finally, the model with the parameter pair (t, m) having the minimal error (on the separate test set) is
202 chosen in order to make the predictions.

203 **2.6 Data availability**

204 All data used in this paper (including the image and RSML libraries) are available at the address
205 <http://doi.org/10.5281/zenodo.208214>

206 An archived version of the codes used in this paper is available at the address
207 <http://doi.org/10.5281/zenodo.208499>

208 An archived version of the machine learning framework is available at the address
209 <https://github.com/FaustFrankenstein/RandomForestFramework/releases/tag/v1.0>

210

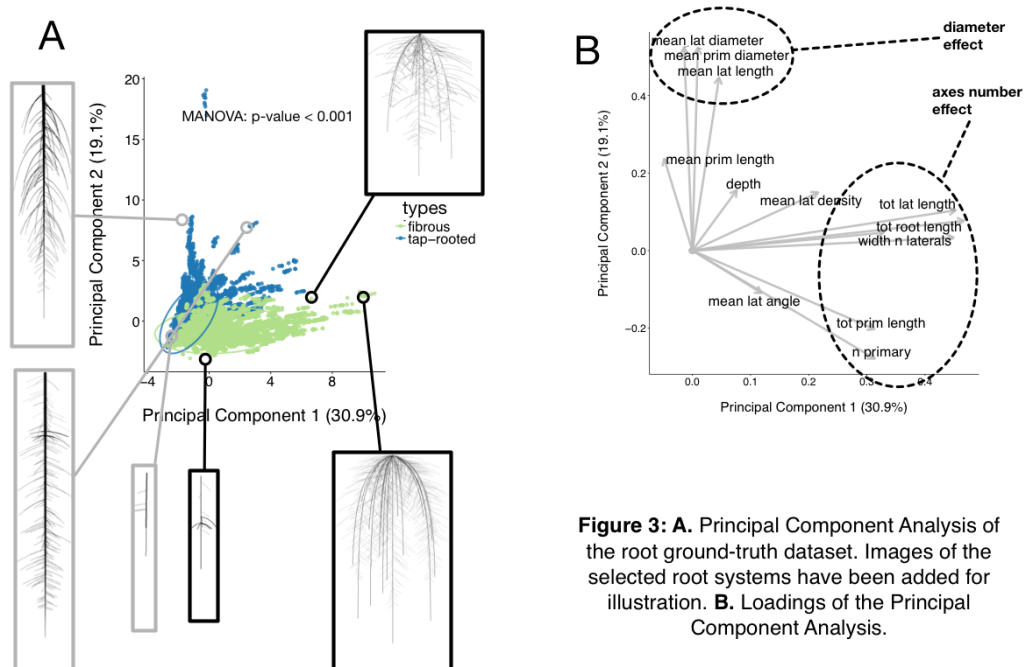
211 3 Results and discussions

212 3.1 Production of a large library of ground-truth root system images

213 We combined existing tools into a single pipeline to produce a large library of ground-truth root
214 system images. The pipeline combines a root model (ArchiSimple (Pagès et al., 2013)), the Root
215 System Markup Language (RSML) and the RSML Reader plugin from ImageJ (Lobet et al., 2015).
216 In short, ArchiSimple was used to create a large number of root systems, based on random input
217 parameter sets. Each output was stored as an RSML file (fig. 2A), which was then used by the RSML
218 Reader plugin to create a graphical representation of the root system (as a .jpeg file) and a ground-
219 truth dataset (fig. 2B). Details about the different steps are presented in the Materials and Methods
220 section.

221 We used the pipeline to create a library of 10,000 root system images, separated into fibrous
222 (multiple first order roots and no secondary growth) and tap-root systems (one first order root and
223 secondary growth). The ranges of the different ground-truth data are shown in table 3 and their
224 distribution is shown in the Supplemental Figure 1.

225 We started by evaluating whether fibrous and tap-root systems should be separated during the
226 analysis. We performed a Principal Component Analysis on the ground-truth dataset to reduce its
227 dimensionality and assess if the *type* grouping influenced the overall dataset structure (fig. 3A).
228 Fibrous and tap-root systems formed distinct groups (MANOVA p-value < 0.001), with limited
229 overlap. The first principal component, which represented 30.9% of the variation within the dataset,
230 was mostly influenced by the number of primary axes. The second principal component (19.1% of
231 the variation) was influenced, in part, by the root diameters. These two effects were consistent with
232 the clear root system type grouping, since they expressed the main difference between the two groups
233 of root-system *types*. Therefore, since the *type* grouping had such a strong effect on the overall
234 structure, we decided to separate them for the following analyses.



235
236
Figure 3: A. Principal Component Analysis of the root ground-truth dataset. Images of the selected root systems have been added for illustration. **B.** Loadings of the Principal Component Analysis.

237 3.2 Systematic evaluation of root image descriptors

238 To demonstrate the utility of a synthetic library of ground-truth root systems, we analysed every
 239 image of the library using a custom-built root image analysis tool, RIA-J. We decided to do so since
 240 our purpose was to test the usefulness of the synthetic analysis and not to assess the accuracy of
 241 existing tools. Nonetheless, RIA-J was designed using known and published algorithms, often used in
 242 root system quantification. A detailed description of RIA-J can be found in the Materials and
 243 Methods section and Supplemental File 1.

244 We extracted 10 descriptors from each root system image (Table 2) and compared them with their
 245 own ground-truth data. For each pair of descriptor-data, we performed a linear regression and
 246 computed its r-squared value. Figure 4 shows the results from the different combinations for both
 247 root system types. We can observe that, generally, correlations were poor with only 3% of the
 248 combinations having an r-squared above 0.8. In addition, for some ground-truth data, such as the
 249 mean lateral length or the number of primary roots, none of the descriptors actually gave a good
 250 estimation (fig 4, highlighted with arrows).

251

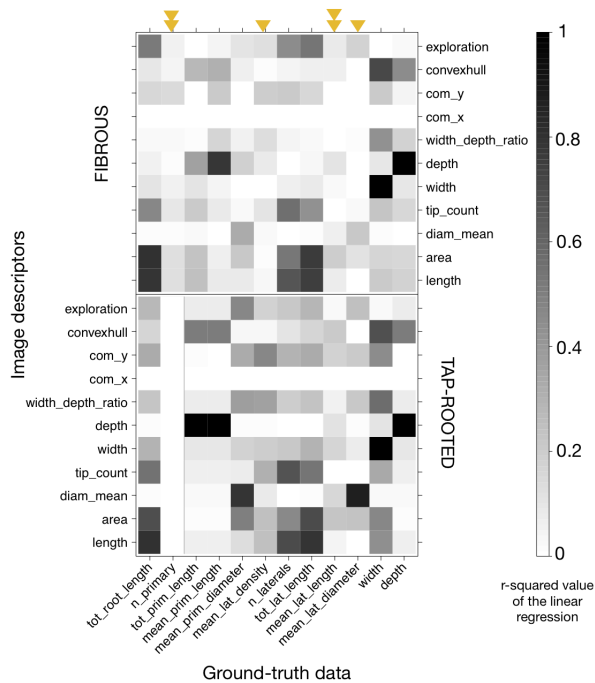


Figure 4: Heatmap of the r-squared values between the different image descriptors and the ground-truth values, for the images without any noise. Black represents an r-squared value of 1; white represents a value of 0. Upper panel: tap-root dataset. Lower panel: fibrous root dataset. Arrows highlight the ground-truth data that can not be accurately described with the different descriptors. The arrows were doubled when it was the case for both fibrous and tap-rooted root systems.

252

253 Additionally, it should be noted that the correlations were different for fibrous- and tap-root systems.
 254 As an example, the correlation found between the *mean_lat_diameter* and *diam_mean* estimators was
 255 better for fibrous roots than within the tap-root dataset. Consequently, validation of the different
 256 image analysis algorithms should be performed, at least, for each group. An algorithm giving good
 257 results for a fibrous root system might fail when applied to tap-rooted ones.

258

259 **3.3 Errors from image descriptors are likely to be non-linear across root system sizes and** 260 **image qualities**

261 In addition to being related to the species of study, estimation errors are likely to increase with the
262 root system size. As the root system grows and develops, the number of crossing and overlapping
263 segments increases (fig. 5A), making the subsequent image analysis potentially more difficult and
264 prone to error. However, a systematic analysis of such error is seldom performed.

265 Figure 5 shows the relationship between the ground-truth and descriptor values for three parameters:
266 the total root length (fig. 5B), the number of roots (fig. 5C) and the root system depth (fig. 5D). For
267 each of these variables, we quantified the Mean Relative Error (see Materials and Methods for
268 details) as a function of the overlap index. This was done for three levels of noise added to the
269 images (“null”, “medium” and “high”). We can observe that for the estimation of both the total root
270 length and the number of lateral roots, the Mean Relative Error increased with the size of the root
271 system (fig. 5B-C). As stated above, such increase of the error was somehow expected with
272 increasing complexity. Moreover, depending on the metric of interest, such as the number of root
273 tips, low image quality can result in high level of error. For other traits, such as the root system
274 depth, no errors were expected (*depth* is supposedly an error-less variable) and the Mean Relative
275 Error was close to 0 whatever the size of the root system and image quality.

276 The results presented here are tightly dependent on the specific algorithms used for image analysis
277 and hence might be different for other published tools. However, they are a call for caution when
278 analysing root images : unexpected errors in ground-truth estimation can arise. Our image library can
279 be used to better identify the errors generated by other analysis tools, current or future.

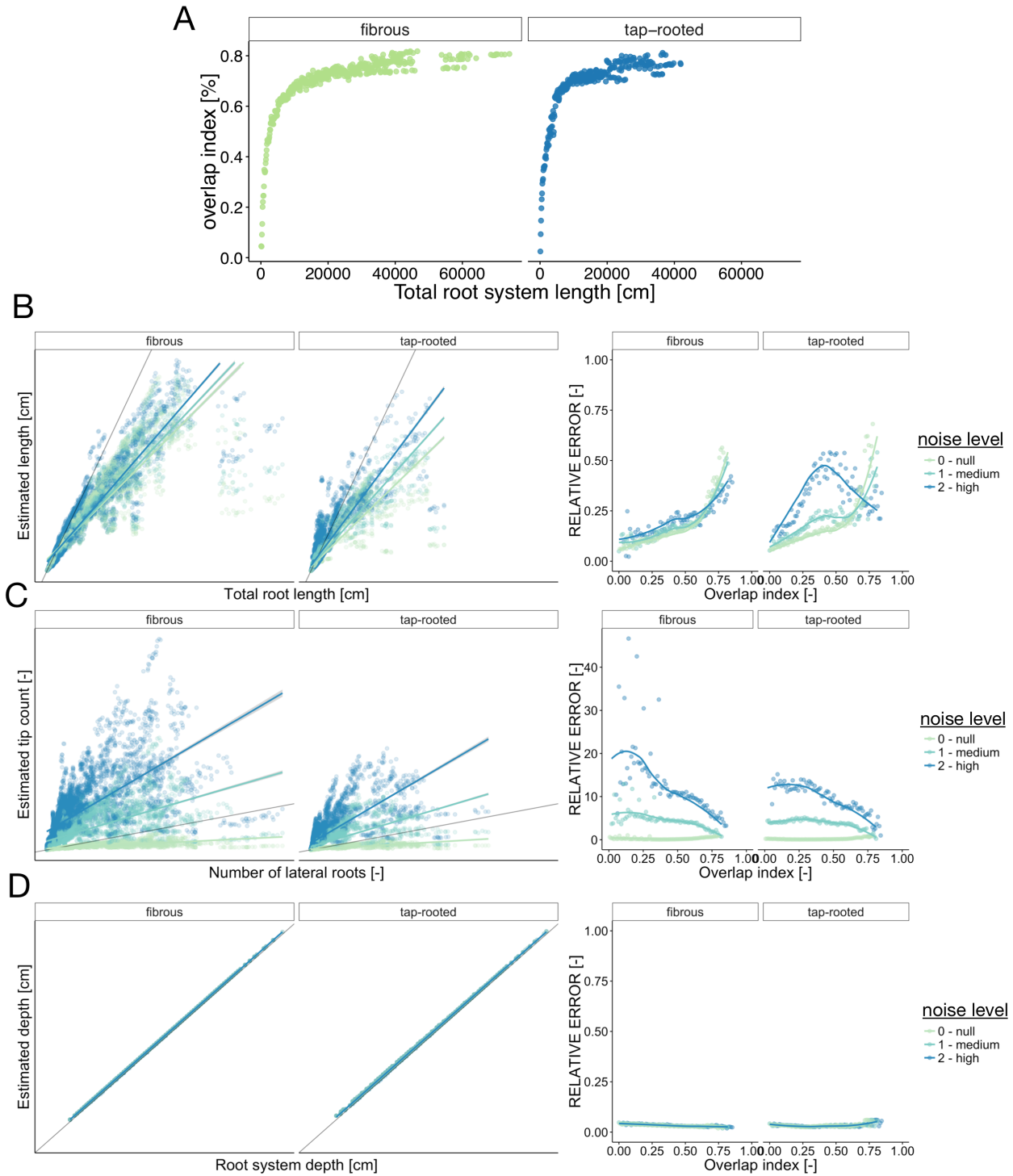


Figure 5: Error estimation for three ground-truth parameters. A. Evolution of the overlap index (proportion of root overlapping) with the root system size. B-D: Left panel shows the relationship between the descriptors and the corresponding ground-truth variables. Right panels show the evolution of the Mean Relative Error (MRE) as a function of the overlap index. For the MRE calculations, the continuous variables were discretized in groups. B. Total root length. C. Number of lateral roots. D. Root system depth

281 3.4 Using the synthetic library to train machine learning algorithms

282 The main advantage of creating a synthetic library is to generate paired datasets of image descriptors and their
 283 corresponding ground-truth values. Having both information can, in theory, be used to either calibrate the
 284 image analysis pipeline or to identify the best descriptors for the ground-truth traits of interest. Here, we
 285 explored the second approach and used a random forest algorithm to find which combination of descriptors
 286 would best describe each ground-truth data (see Material and Methods for details). In short, we randomly
 287 divided the whole dataset into training (3/4) and testing subsets (1/4). The training set was used to create a
 288 random forest model for each ground-truth data, which was then we applied to the test set. The accuracy of
 289 these new predictions was then compared to the accuracy of the direct method (single descriptors) (fig. 2C).

290 Figure 6 shows the comparison of the accuracy (both the r-squared values from linear regressions and the
 291 Mean Relative Error, MRE) of both methods for each ground-truth data. We can clearly see that the random
 292 forest approach performed always better (sometimes substantially) than the direct approach, even for images
 293 with high level of noise. In addition, for most traits, the r-squared and MRE values were above 0.9 and below
 294 0.1 respectively, which is very good, especially for such a wide range of images. In addition, the random forest
 295 approach allowed the correct estimation of traits that were difficult to estimate with the direct approach (such
 296 as the number of primary axes or the mean lateral root density).

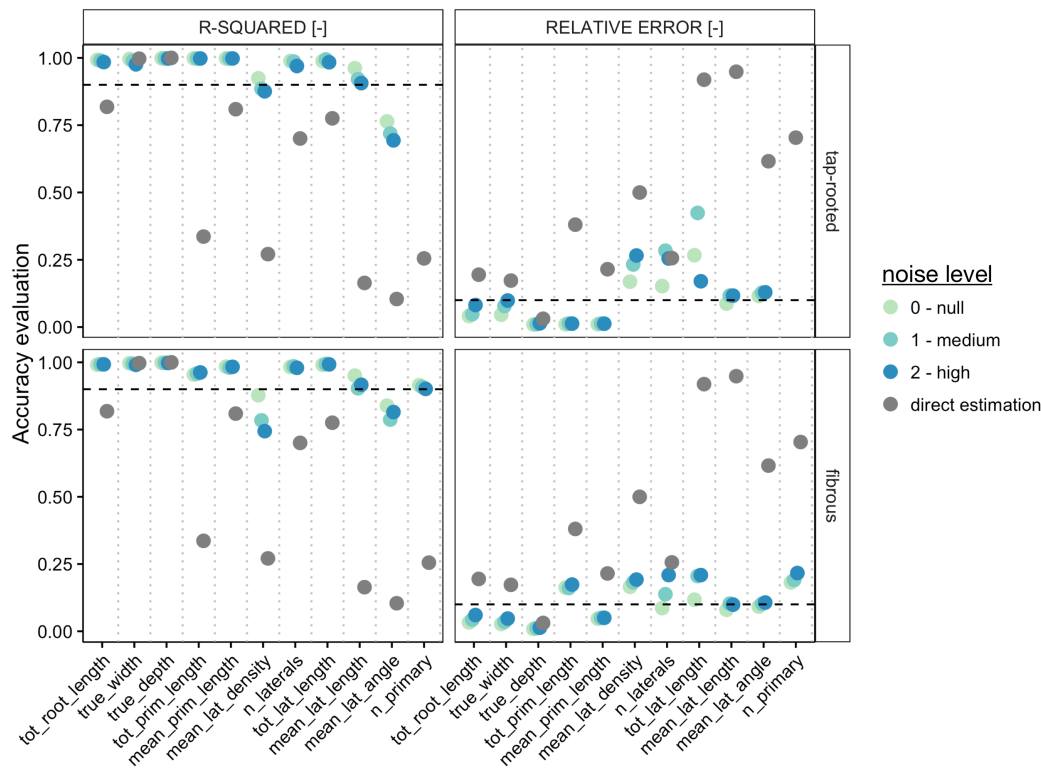


Figure 6: Comparison between the direct trait and the random forest approach, for the different root system types and the different levels of noise. For each metric, we computed both the r-squared value from the linear regression between the estimation and the ground-truth (left panels), as well as the Mean Relative Error (right panel). The grey points represent the values obtained with the direct estimation (best descriptor, no noise). Color points represent the values obtained with the random forest approach, for different levels of noise. The dotted lines show the 0.9 (r-squared) and 0.1 (MRE) thresholds.

298 Figure 7 shows the detailed comparison of both methods for the estimation of the total root length. Again, a
299 clear improvement was visible with the Random Forest method, leading to small errors, even with large root
300 systems and noisy images.

301 In our study, machine learning algorithms on simulated datasets seems to yield very good results and we
302 believe they open new avenues for root system analyses. It is clear however that their value relies on the
303 quality and relevance of the training dataset vs. the test dataset and that they must be carefully designed.

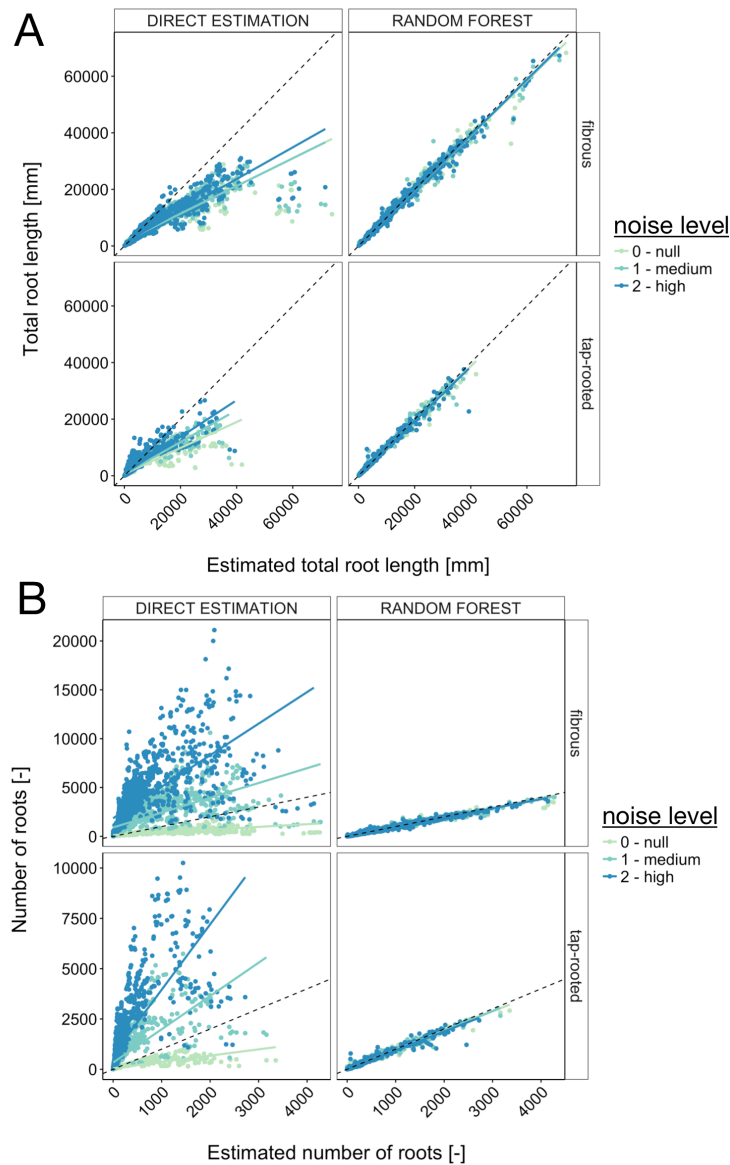


Figure 7: Comparison between the direct trait estimation and the random forest approach, for the different root system types and the different levels of noise. A. Comparison, for the total root length, of the accuracy of both approaches. The dotted line represents the diagonal. The plain line represents the linear regression. B. Same, for the number of roots.

305 4 Conclusions

306 The automated analysis of root system images is routinely performed in many research projects. Here
307 we used a library of 10;000 synthetic images to estimate the accuracy and usefulness of different
308 image descriptors extracted with a homemade root image analysis pipeline. Our study highlighted
309 some limitations and biases of the image analysis process.

310 We found that the type of root system (fibrous vs tap-rooted), its size and complexity, as well as the
311 quality of the images had a strong influence on the accuracy of some commonly used image
312 descriptors and their meaning and relevance for ground-truth extraction. So far, a large proportion of
313 the root research has been focused on seedlings with small root systems and has *de facto* avoided
314 such errors.

315 However, as the research questions are likely to focus more on mature root systems in the future,
316 these limitations will become critical. We showed that synthetic datasets can be used for calibration
317 or modelling (machine learning) steps that allow ground-truth extraction from comparable images.
318 We then hope that our library will be helpful for the root research community to evaluate and
319 improve other image analysis pipelines.

320

321 **5 Conflict of Interest**

322 The authors declare that the research was conducted in the absence of any commercial or financial
323 relationships that could be construed as a potential conflict of interest.

324

325 **6 Author Contributions**

326 GL, LP, PT, IK, MN and CP designed the study. IK developed the image analysis pipeline RIA-J.
327 MN and PM developed the Random Forest framework. GL generated the image library and did the
328 data analysis. LP developed the Archisimple model. All authors have participated in the writing of
329 the manuscript.

330

331 **7 Funding**

332 This research was funded by the Interuniversity Attraction Poles Programme initiated by the Belgian
333 Science Policy Office, P7/29. GL and MN are grateful to the F.R.S.-FNRS for a postdoctoral
334 research grant (1.B.237.15F) and doctoral grant (1.A.320.16F), respectively.

335

336 **8 Supplementary Material**

337 - **Supplemental figure 1:** Distribution of the properties of the modelled root images

338 - **Supplemental figure 2:** Distribution of the descriptors of the modelled root images

339 - **Supplemental file 1:** Definitions of the different descriptors extracted by RIA-J

340

341 **9 Figures legends**

342 **Figure 1:**

343 A. Image of a 2-week old maize root system grown in rhizotron. B. Close-up showing overlapping
344 roots. C. Close-up showing crossing roots.

345 **Figure 2:**

346 Overview of the workflow used in this study. A. Generation of root systems using Archisimple. B.
347 Creation and analysis of root images. C. Use of Random Forest algorithms to better estimate root
348 system ground-truths. D. Illustration of the different noise levels used in the analysis. E. Example of
349 descriptors extracted with RIA-J

350 **Figure 3:**

351 A. Principal Component Analysis of the root ground-truth dataset. Images of the selected root
352 systems have been added for illustration. B. Loadings of the Principal Component Analysis.

353 **Figure 4:**

354 A. Heatmap of the r-squared values between the different image descriptors and the ground-truth
355 values, for the images without any noise. Black represents an r-squared value of 1; white represents a
356 value of 0. Upper panel: tap-root dataset. Lower panel: fibrous root dataset. Arrows highlight the
357 ground-truth data that cannot be accurately described with the different descriptors. The arrows were
358 doubled when it was the case for both fibrous and tap-rooted root systems.

359 **Figure 5:**

360 Error estimation for three ground-truth parameters. A. Evolution of the overlap index (proportion of
361 root overlapping) with the root system size. B-D: Left panel shows the relationship between the
362 descriptors and the corresponding ground-truth variables. Right panels show the evolution of the
363 Mean Relative Error (MRE) as a function of the overlap index. For the MRE calculations, the
364 continuous variables were discretized in groups. B. Total root length. C. Number of lateral roots. D.
365 Root system depth

366 **Figure 6:**

367 Comparison between the direct trait and the random forest approach, for the different root system
368 types and the different levels of noise. For each metric, we computed both the r-squared value from
369 the linear regression between the estimation and the ground-truth (left panels), as well as the Mean
370 Relative Error (right panel). The grey points represent the values obtained with the direct estimation
371 (best descriptor, no noise). Color points represent the values obtained with the random forest
372 approach, for different levels of noise. The dotted lines show the 0.9 (r-squared) and 0.1(MRE)
373 thresholds.

374 **Figure 7:**

375 Comparison between the direct trait estimation and the random forest approach, for the different root
376 system types and the different levels of noise. **A.** Comparison, for the total root length, of the

377 accuracy of both approaches. The dotted line represents the diagonal. The plain line represents the
378 linear regression. **B.** Same, for the number of roots.

379

380

381 **10 Tables**

382 **Table 1:** Root system parameters used as ground-truth data

Name	Description	Unit
tot_root_length	The cumulative length of all roots	mm
tot_prim_length	The cumulative length of all root axes	mm
tot_lat_length	The cumulative length of all lateral roots	mm
mean_prim_length	The mean first-order roots length	mm
mean_lat_length	The mean lateral root length	mm
n_primary	The total number of first order roots	-
n_laterals	The total number of lateral roots	-
mean_lat_density	The mean lateral root density: for each first-order root, the number of lateral roots divided by the axis length (total length).	mm ⁻¹
mean_prim_diam	The mean diameter of the first-order roots	mm
mean_lat_diam	The mean diameter of the lateral roots	mm
mean_lat_angle	The mean insertion angle of the lateral roots	°

383

384

385 **Table 2:** Root image descriptors extracted by RIA-J

Name	Description	Unit	Reference
Morphology			
area	Projected area of the root system	mm ²	(Galkovskyi et al., 2012)
length	Length of the skeleton of the root system image	mm	(Galkovskyi et al., 2012)
tip_count	Number of end branches in the root system skeleton	-	
diam_mean	Mean diameter of the root object in the image	mm	
Geometry			
width	The maximal width of the root system	mm	-
depth	The maximal depth of the root system	mm	-
width_depth_ratio	Ratio between the width and the depth of the root system	-	(Galkovskyi et al., 2012)
com_x - com_y	Relative coordinates of the centre of mass of the root system	-	(Galkovskyi et al., 2012)
convexhull	Area of the smallest convex shape encapsulating the root system	mm ²	(Galkovskyi et al., 2012)
exploration	Ratio between the convex hull area and the projected area	-	(Galkovskyi et al., 2012)

387 **Table 3:** Ranges of the different ground-truth data from the root systems generated using
 388 ArchiSimple

variable	minimum value	maximum value	unit
Fibrous			
tot_root_length	110	73971	mm
width	0.76	302	mm
depth	50	505	mm
n_primary	1	20	-
tot_prim_length	79	5409	mm
mean_prim_length	27	470	mm
mean_prim_diameter	0.2	0.4	mm
mean_lat_density	0	5	root/mm
n_laterals	0	4448	-
tot_lat_length	0	71556	mm
mean_lat_length	0	50	mm
mean_lat_diameter	0	0.3	mm
mean_lat_angle	0	88	°
Tap rooted			
tot_root_length	78	41870	mm
width	0.1	173	mm

depth	55	505	mm
n_primary	1	1	-
tot_prim_length	59	509	mm
mean_prim_length	59	509	mm
mean_prim_diameter	0.2	16	mm
mean_lat_density	0	2.3	root/mm
n_laterals	0	3353	-
tot_lat_length	0	40225	mm
mean_lat_length	0	51	mm
mean_lat_diameter	0	2.2	mm
mean_lat_angle	0	97	°

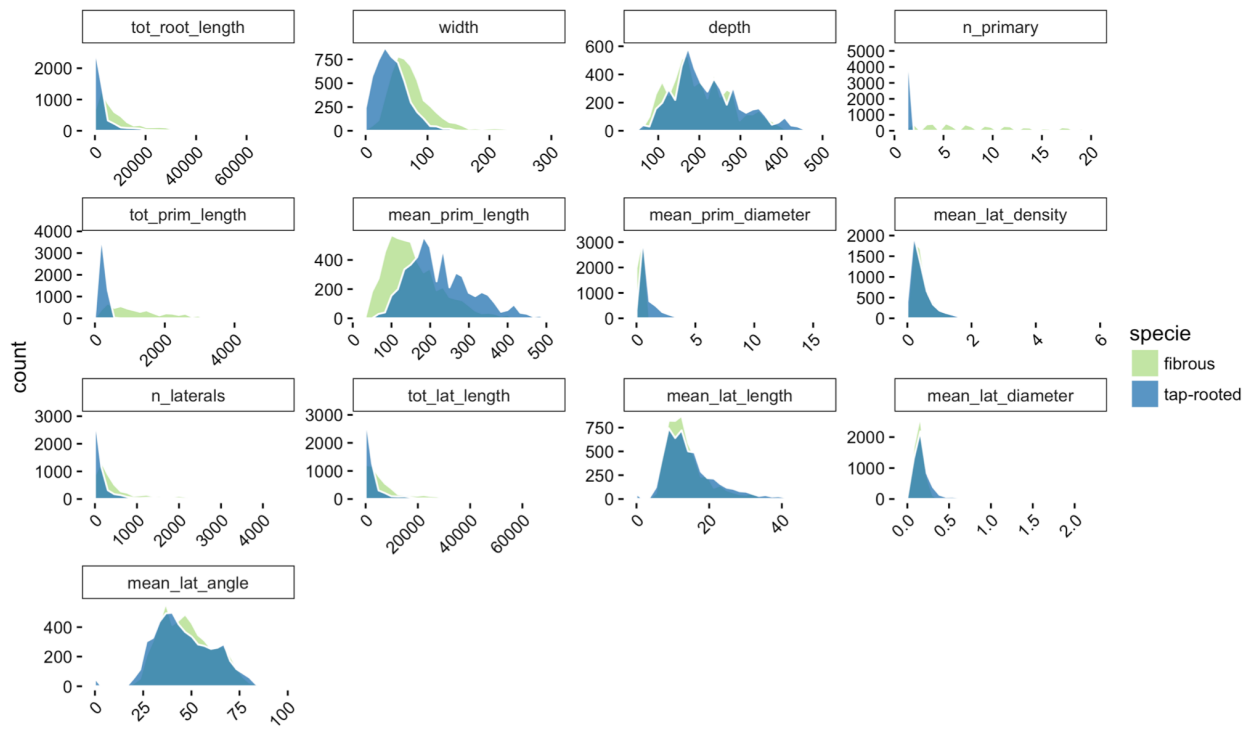
389

390

391 **11 References**

- 392 Armengaud, P., Zambaux, P., Hills, A., Sulpice, R., Pattison, R. J., Blatt, M. R., et al. (2009). EZ-
393 Rhizo: integrated software for the fast and accurate measurement of root system architecture. *Plant J*
394 *57*, 945–956.
- 395 Benoit, L., Rousseau, D., Belin, É., Demilly, D., and Chapeau-Blondeau, F. (2014). Simulation of
396 image acquisition in machine vision dedicated to seedling elongation to validate image processing
397 root segmentation algorithms. *Computers and Electronics in Agriculture* *104*, 84–92.
- 398 Bonhomme, V., Picq, S., and Gaucherel, C. (2014). Momocs: outline analysis using R. *Journal of*
399 *Statistical ...*
- 400 Breiman, L (2001). Random Forests. *Machine Learning*. **45** (1): 5–32
- 401 Breiman, L (1996). Bagging predictors. *Machine Learning*. **24** (2): 123–140.
- 402 Bucksch, A., Burrridge, J., York, L. M., Das, A., Nord, E., Weitz, J. S., et al. (2014). Image-based
403 high-throughput field phenotyping of crop roots. *Plant Physiol*. *166*, 470–486.
- 404
- 405 Chitwood, D. H., and Otoni, W. C. (2016). Morphometric analysis of Passiflora leaves I: the
406 relationship between landmarks of the vasculature and elliptical Fourier descriptors of the blade.
407 *bioRxiv*.
- 408 CRAN randomForest (2015). [https://cran.r-](https://cran.r-project.org/web/packages/randomForest/randomForest.pdf)
409 [project.org/web/packages/randomForest/randomForest.pdf](https://cran.r-project.org/web/packages/randomForest/randomForest.pdf)
- 410 Dryden, I. L. (2015). shapes package. Vienna, Austria.
- 411 Galkovskyi, T., Mileyko, Y., Bucksch, A., Moore, B., Symonova, O., Price, C. A., et al. (2012). GiA
412 Roots: software for the high throughput analysis of plant root system architecture. *BMC Plant Biol*
413 *12*, 116.
- 414 Huynh-Thu, V. A., Wehenkel, L, & Geurts, P. (2013) Gene regulatory network inference from
415 systems genetics data using tree-based methods.
- 416 Koevoets, I. T., Venema, J. H., Elzenga, J. T. M., and Testerink, C. (2016). Roots Withstanding their
417 Environment: Exploiting Root System Architecture Responses to Abiotic Stress to Improve Crop
418 Tolerance. *Front Plant Sci* *07*, 91–19.
- 419 Lobet, G., Pound, M. P., Diener, J., Pradal, C., Draye, X., Godin, C., et al. (2015). Root System
420 Markup Language: Toward a Unified Root Architecture Description Language. *Plant Physiol* *167*,
421 617–627.
- 422 Marée, R., Geurts, P., & Wehenkel, L. (2016). Towards Generic Image Classification using Tree-
423 based Learning: an Extensive Empirical Study. *Pattern Recognition Letters*.
- 424 Pagès, L., and Pellerin, S. (1996). Study of differences between vertical root maps observed in a
425 maize crop and simulated maps obtained using a model for the three-dimensional architecture of the
426 root system. *Plant and Soil* *182*, 329–337.

- 427 Pagès, L., Bécel, C., Boukcim, H., Moreau, D., Nguyen, C., and Voisin, A.-S. (2013). Calibration
428 and evaluation of ArchiSimple, a simple model of root system architecture. *Ecological Modelling*
429 290, 76–84.
- 430 Pagès, L., Jordan, M. O., and Picard, D. (1989). A simulation model of the three-dimensional
431 architecture of the maize root system. *Plant and Soil* 119, 147–154.
- 432 Pagès, L., Vercambre, G., Drouet, J.-L., Lecompte, F., Collet, C., and LeBot, J. (2004). RootTyp: a
433 generic model to depict and analyze the root system architecture. *Plant and Soil* 258, 103–119.
- 434 Pierret, A., Gonkhamdee, S., Jourdan, C., and Maeght, J.-L. (2013). IJ-Rhizo: an open-source
435 software to measure scanned images of root samples. *Plant and Soil*, 1–9.
- 436 R Core Team R: A Language and Environment for Statistical Computing.
- 437 Rellán-Álvarez, R., Lobet, G., Lindner, H., Pradier, P.-L., Sebastian, J., Yee, M.-C., et al. (2015).
438 GLO-Roots: an imaging platform enabling multidimensional characterization of soil-grown root
439 systems. *eLife* 4, e07597.
- 440 Ristova, D., Rosas, U., Krouk, G., Ruffel, S., Birnbaum, K. D., and Coruzzi, G. M. (2013).
441 RootScape: A landmark-based system for rapid screening of root architecture in *Arabidopsis thaliana*.
442 *Plant Physiology*
- 443 Sarkar, D. (2008). *Lattice: Multivariate Data Visualization with R*. New York: Springer.
- 444 Wickham, H. (2009). *ggplot2*. New York, NY: Springer New York
- 445
- 446

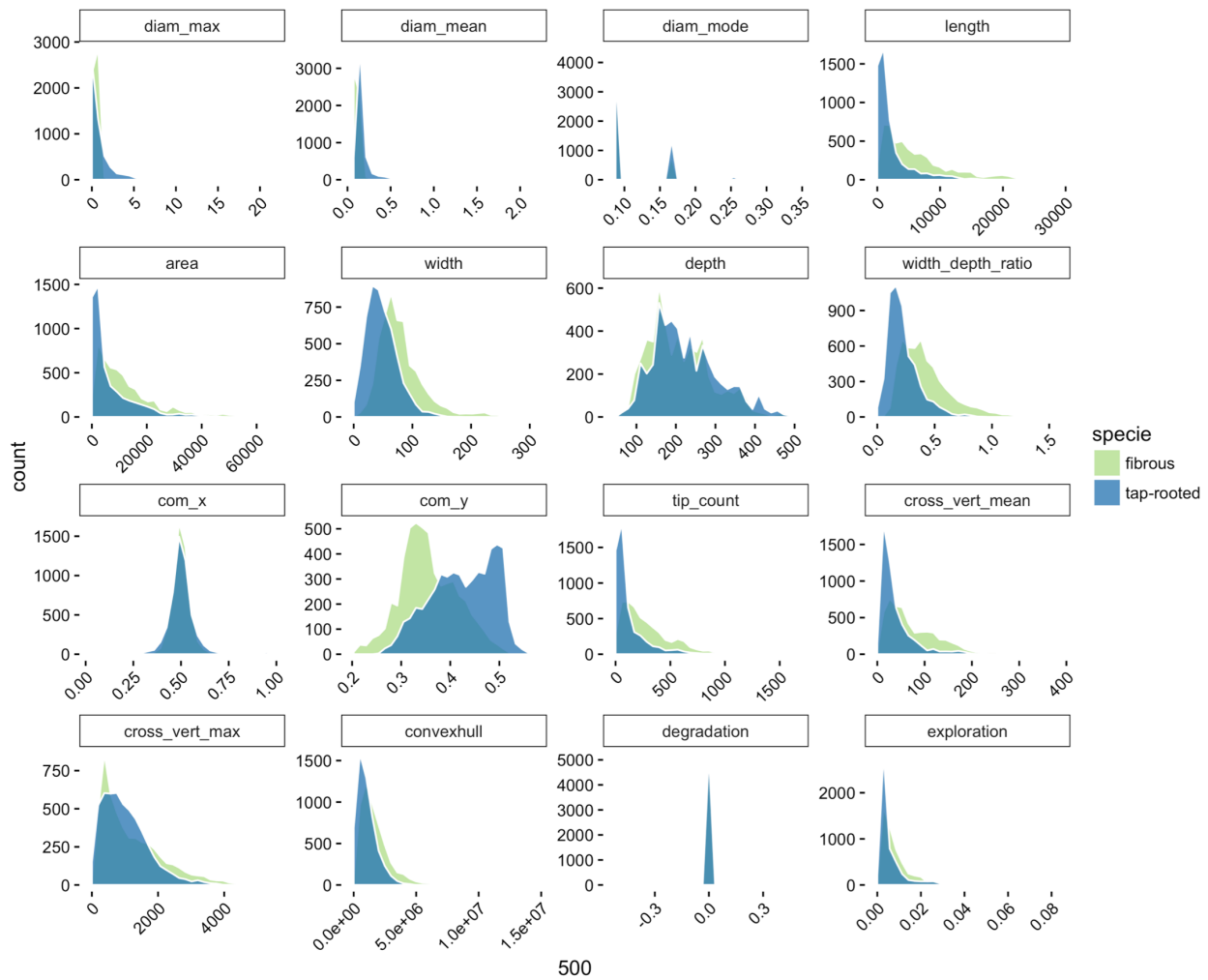


500

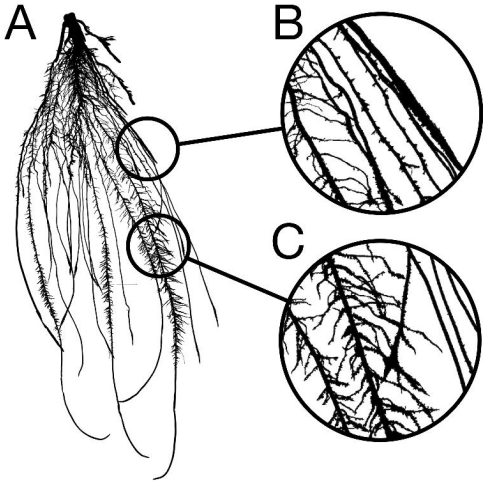
Supplemental figure 1: Distribution of the properties of the modelled root images for fibrous and tap-rooted root systems. X axis represent the range off value for each properties.

447

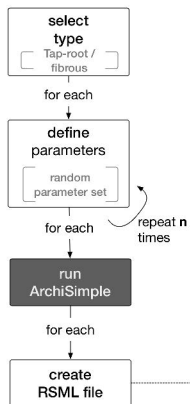
448



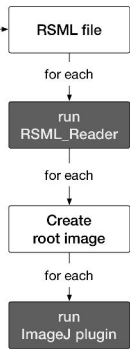
Supplemental figure 2: Distribution of the descriptors of the modelled root images for fibrous and tap-rooted root systems. X axis represent the range off value for each properties.



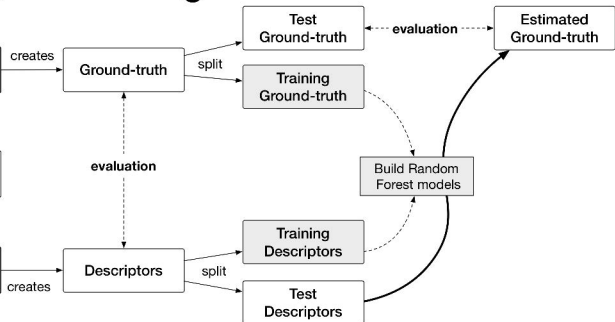
A



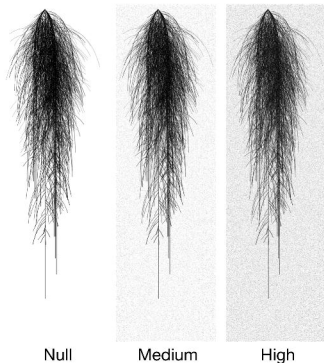
B



C



D



E

